

The photodissociation dynamics of ozone at 226 and 248 nm: $O(^3P_J)$ atomic angular momentum polarization

M. Brouard,^{a)} A. Goman, S. J. Horrocks, A. J. Johnsen, F. Quadrini, and W.-H. Yuen
*The Physical and Theoretical Chemistry Laboratory, The Department of Chemistry, University of Oxford,
 South Parks Road, Oxford OX1 3QZ, United Kingdom*

(Received 23 July 2007; accepted 6 September 2007; published online 8 October 2007)

Speed distributions, and spatial anisotropy and atomic angular momentum polarization parameters have been determined for the $O(^3P_J)$ products following the photodissociation of ozone at 248 and 226 nm using velocity map ion imaging. The data have been interpreted in terms of two dissociation mechanisms that give rise to fast and slow products. In both cases, excitation is believed to occur to the \tilde{B} state. Consistent with previous interpretations, the speed distributions, translational anisotropy parameters, and angular momentum polarization moments support the assignment of the major pathway to curve crossing from the \tilde{B} to the repulsive \tilde{R} surface, generating fast fragments in a wide range of vibrational states. For the slow fragments, it is proposed that following excitation to the \tilde{B} state, the system crosses onto the \tilde{A} state. The crossing seam is only accessible to molecules that are highly vibrationally excited and therefore possess modest recoil speeds. Once on the \tilde{A} state, the wavepacket is thought to funnel through a conical intersection to the ground state. The velocity distributions, spatial anisotropy parameters, spin-orbit populations and polarization data each lend support to this mechanism. © 2007 American Institute of Physics. [DOI: 10.1063/1.2790890]

I. INTRODUCTION

Ground state triplet products constitute only a minor channel in the Hartley band dissociation of ozone. The quantum yield for $O(^3P_J)$ production is about 0.1,^{1–5} compared with around 0.9 for the singlet product channel, $O(^1D_2) + O_2(a^1\Delta_g)$. From an early stage, the pathway leading to $O(^3P_J) + O_2(X^3\Sigma_g^-)$ products was identified by Hay *et al.*⁶ as proceeding via excitation to the \tilde{B} state, with subsequent crossing onto the \tilde{R} state repulsive surface (see Fig. 1). Interest in the triplet product channel was awakened when a number of groups proposed that production of highly vibrationally excited $O_2(X^3\Sigma_g^-)$, born with a sufficient amount of vibrational excitation ($v_{O_2} \geq 26$), might hold the key to the “ozone deficit problem.”^{7–9} As a result, a number of laboratory studies on the triplet channel dissociation of ozone were undertaken, with the intention of establishing the existence and quantum yield of vibrationally excited $O_2(X^3\Sigma_g^-)$.^{10–18} The ozone deficit problem and its proposed solution remain as controversial issues.^{19–22} Nevertheless, the presence of a bimodal $O_2(X^3\Sigma_g^-)$ vibrational distribution produced in the photolysis of ozone via the Hartley band has been unambiguously demonstrated,¹⁰ and its dynamical origin is still largely unexplained.

Although early works by Fairchild *et al.*¹ and Sparks *et al.*³ identified the existence of a triplet dissociation channel by studying the kinetic energy release of oxygen atoms following dissociation in the Hartley band, Kinugawa *et al.*²³ presented the first study of the dynamics of triplet formation resolved in atomic spin-orbit state. By selectively ionizing

the $O(^3P_J)$ atoms via a resonantly enhanced multiphoton ionization (REMPI) transition near 226 nm, the authors were able to collect time-of-flight (TOF) profiles for these products following dissociation at the probe wavelength. The kinetic energy distributions were reported to be broad, indicating that a wide range of vibrational states was populated in the O_2 cofragment. A peak corresponding to slow O atoms

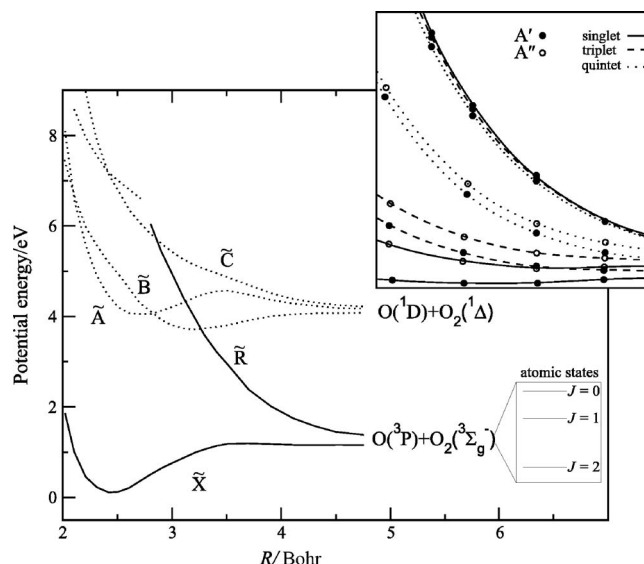


FIG. 1. Cut through the lowest five $^1A'$ surfaces for ozone adapted from Ref. 69 with one O–O distance fixed at 1.3 Å and the bond angle at its ground state equilibrium value of 117°. Potentials are labeled according to the notation of Hay *et al.* (Ref. 6). Relative energy ordering of the $O(^3P_J)$ spin-orbit states is also shown. Top right panel: Singlet, triplet, and quintet molecular states of A' and A'' symmetries as a function of one O–O bond distance, $2.3 \text{ Å} < R_1 < 2.9 \text{ Å}$ (4.3–5.5 bohrs) with other coordinates fixed at their ground state equilibrium values. Adapted from Ref. 36.

^{a)}Electronic mail: mark.brouard@chem.ox.ac.uk

was observed by these authors, but this was attributed primarily to signal arising from thermal oxygen atoms generated by catalytic degradation of ozone. Park and Slinger²⁴ subsequently estimated the nascent O_2 vibrational state populations following dissociation at 248 nm by using laser induced fluorescence (LIF). The nascent vibrational population of O_2 molecules obtained from those measurements was found to be in broad agreement with the distribution recovered by Kinugawa *et al.*²³ Daniels and Wiesenfeld²⁵ measured the rotational distributions of the $O_2(X^3\Sigma_g^-)$ photofragments born with 9, 12, and 15 quanta of vibrational excitation produced from the dissociation of ozone at 248 nm. The distributions were found to peak at values of $f_{rot}=0.15$, consistent with an impulsive model, in which dissociation was assumed to occur from the ground electronic state equilibrium geometry. Shamsuddin *et al.*²⁶ measured the O-atom spin-orbit populations following dissociation at 266 nm to be almost exactly statistical. The result was seen to indicate that diabatic dissociation dominates the exit channel of the triplet forming pathway. This Doppler-resolved vacuum ultraviolet LIF study was also sensitive to the spin-orbit dependent β parameters, which were found to be 0.83, 0.75, and 0.65 for $J=2$, 1, and 0, respectively, in very good agreement with previous measurements by Kinugawa *et al.*²³ The authors argued that their results could be interpreted in terms of a prompt dissociation from a bond angle of 102° .

Miller *et al.*¹⁰ and, later, Syage^{11–13} reinvestigated the triplet forming channel in a set of one-color experiments at the $O(^3P_J)$ probe wavelength of 226 nm. Using a combination of LIF measurements and photofragment ion imaging, Miller *et al.* were the first to unambiguously assign the slow $O(^3P_J)$ products as arising from the photolysis of ozone and specifically to the production of $O_2(X^3\Sigma_g^-)$ cofragments born in $v_{O_2}\geq 26$, with a partial quantum yield of just under 1%. Spin-orbit branching ratios were also measured and found to be nearly statistical, mirroring the results of Shamsuddin *et al.*²⁶ at 266 nm. Syage^{11–13} reported similar results from a series of core-extracted REMPI TOF measurements. These workers obtained a β value for the main feature in the speed distribution of 1.2, close to the value for the singlet channel following excitation into the Hartley band. For the slow, vibrationally excited products β was found to be 0.4.

Houston and co-workers extended the imaging work of Miller *et al.*¹⁰ to a range of wavelengths between 226 and 266 nm.^{14,17,18} In agreement with previous work, O-atom spin-orbit branching ratios were found to be insensitive to wavelength and in general close to the statistical limit. Consistent with the nascent $O_2(X^3\Sigma_g^-)$ vibrational distribution measured by Hickson *et al.* at 266 nm,¹⁶ Geiser *et al.* observed bimodal photofragment kinetic energy release distributions at all dissociation wavelengths up to 266 nm.¹⁷ They argued that the persistence of a bimodal speed distribution at this wavelength, which is below the energetic threshold for production of O_2 in $v_{O_2}=26$, might be evidence for the participation of a spin forbidden channel to the dynamics.¹⁷ In agreement with previous works,^{11–13,15} Houston and co-workers also found that at the majority of dissociation wavelengths studied, the β parameter rose steadily from values of around 0.5 at low velocity to large positive values, near 1.5,

for the highest velocities. They also noticed that the population of $O_2(X^3\Sigma_g^-)$ photofragments with $v_{O_2}\geq 26$ decreased with increasing wavelength.^{17,18} In addition to the possibility of triplet channel involvement mentioned above, the authors proposed a tentative model for the dissociation that included two distinct curve crossing regions leading to product flux on the \tilde{R} surface, one near the minimum energy pathway, leading to relatively fast products, and the other where the O–O bond lengths were considerably extended, leading to a “bobsled effect,” and producing highly vibrationally excited products.^{17,18}

Theoretical work on the photodissociation of ozone has recently been reviewed by Grebenshchikov *et al.*²⁷ and is therefore summarized briefly here. Only two attempts to model the dynamics of the triplet channel within the Hartley band have been presented.^{28,29} In 1995, Svanberg *et al.* presented a statistical model to describe the ground state product formation process,²⁸ in which they assumed strong vibrational coupling on the \tilde{B} state up to a critical distance, called the decoupling distance, at which crossing occurs, for example, from the \tilde{B} to the \tilde{R} state. Results from the calculations were compared with the work of Kinugawa *et al.*²³ and Daniels and Wiesenfeld.²⁵ Agreement was found to be profoundly dependent on the choice of decoupling distance. The authors argued that a long-lived complex might be a precursor to triplet product formation, perhaps being connected with the periodic orbits calculated by Leforestier and LeQuéré.³⁰ However, the model was unable to reproduce the slow fragments observed experimentally in the kinetic energy distributions.

A more recent study of the triplet channel was presented by Qu *et al.*,²⁹ in which classical trajectory surface hopping methods were employed to determine speed and product state distributions for the nascent $O(^3P_J)$ fragments. The trajectories were allowed to evolve on the diabatic \tilde{B} state until a crossing with the \tilde{R} state was reached. The model explicitly neglected trapped trajectories^{31–34} that, having passed the crossing region once, did not “hop” onto the \tilde{R} state. The calculated kinetic energy distribution was found to be in good agreement with the experimental results of Geiser *et al.*¹⁷ However, the calculations failed to reproduce the low kinetic energy peak corresponding to $O_2(X^3\Sigma_g^-)$ ($v_{O_2}\geq 26$) identified in earlier experimental studies. In a previous publication,³⁵ the authors had postulated that a series of surface crossings involving the \tilde{B} , \tilde{A} , and \tilde{R} states, not considered in the classical analysis discussed here, could be responsible for the highly vibrationally excited $O_2(X^3\Sigma_g^-)$ products.³⁵

Potential energy surfaces for the states correlating with ground state products have recently been calculated by Rosmus *et al.*³⁶ They focused on the intermediate range region up to 3 Å, where the energy ordering of the singlet electronic states was found to be $1^1A'(^1\Pi) < 1^1A''(^1\Pi) < 2^1A'(^1\Sigma_g^+)$. The study concluded that, at bond angles near 160° , states of singlet, triplet, and quintet spin multiplicities change energy ordering and strongly interact. The spin contamination that ensues was found to be considerable, so that in this region S ,

the spin quantum number is not valid. Similar sets of potential energy surfaces were also obtained more recently in calculations by Tashiro and Schinke.³⁷ In addition, they performed two-dimensional quantum mechanical scattering calculations of the complex-forming $O(^3P_J) + O_2(X^3\Sigma_g^-)$ process for total angular momentum $J_{\text{tot}}=0$ on all 27 potential energy surfaces, coupled solely by the spin-orbit interaction. The authors concluded that spin-orbit coupling was not important, and that a single surface (adiabatic) calculation, corrected by a simple statistical factor, was sufficient to determine the thermal rate of complex formation.³⁷ Note that of the 27 surfaces correlating with $O(^3P_J) + O_2(X^3\Sigma_g^-)$, only one, the ground electronic state of ozone, is significantly bound.³⁷

In the following, we report a detailed velocity map ion imaging study of the $O(^3P_J)$ photofragments generated by photolysis of ozone at 226 and 248 nm. The particular focus of the work is the determination of atomic angular momentum orientation and alignment parameters. In the next section, we briefly outline the experimental and data analysis procedures employed. In Sec. III, we present $O(^3P_J)$ spin-orbit state-resolved speed distributions and translational anisotropy parameters, as well as a comprehensive set of electronic angular momentum polarization data. The findings are discussed in Sec. IV in the light of previous work and of simple models of the dissociation mechanisms.

II. METHOD

A. Experimental procedures

The experiments were carried out using a standard velocity map³⁸ ion imaging³⁹ apparatus that has been described in detail previously.^{40–46} A 15% of $\sim 1:1$ O_3/O_2 mixture, prepared using a commercial ozonizer, was seeded in He at a backing pressure of ~ 1 bar and expanded through a pulsed nozzle with a 0.5 mm diameter orifice. The molecular beam was collimated by a 1 mm diameter skimmer. The rotational temperature of the skimmed molecular beam was measured to be ~ 25 K.⁴⁵ Further downstream, the molecular beam was passed through a 2 mm hole in the repeller plate of the velocity mapping ion optics assembly and crossed 5 cm away from the nozzle exit by two counter-propagating laser beams. The 248 nm photolysis radiation was provided by an excimer laser, while the probe radiation, operating typically at pulse energies of around $500 \mu\text{J pulse}^{-1}$, was obtained by frequency doubling the output of a neodymium doped yttrium aluminum garnet (Nd:YAG)-pumped dye laser system. The time delay between the two laser pulses was ~ 10 ns. Two lenses of 30 cm focal length were used to focus the radiation onto the molecular beam.

The $O(^3P_J)$ photofragments were probed by $(2+1)$ REMPI via the $3p^3P \leftarrow ^3P_J$ transitions near 226 nm.⁴⁷ During image acquisition, the probe laser wavelength was scanned over the Doppler profile of the $O(^3P_J)$ transitions in order to ensure an equal detection sensitivity for all the product velocities. The oxygen ions were velocity mapped onto an imaging detector consisting of a pair of 75 mm chevron double microchannel plates coupled to a P47 phosphor screen. The image on the phosphor screen was captured by

an intensified charge coupled device camera, electronically gated to the flight time of the detected ions and subsequently sent to a personal computer for signal processing (thresholding, event counting,⁴⁸ and accumulation). Images were averaged over 60 000 laser shots. Velocity calibration of the final images was achieved using one-color images of $O(^3P_J)$ from the photodissociation of O_2 .

In order to extract information on the $O(^3P_J)$ atomic polarization, images were obtained in a variety of pump-probe laser geometries. These included the more usual geometries used previously to extract alignment parameters (in this case of rank $K=2$) and labeled as HH, HV, VH, and VV according to the polarization of the pump and probe lasers lying parallel (H) or perpendicular (V) to the image plane (note that the molecular beam axis is perpendicular to the image plane). Data were also collected in other configurations, including both linearly (with the electric vector of the light at $\pm 45^\circ$ to the TOF axis) and left (L) and right (R) circularly polarized photolysis radiations. The use of such a large number of geometries helped ensure that the moments of the angular momentum distribution could be obtained unambiguously. Pairs of images were collected simultaneously by using a photoelastic modulator to switch the probe laser polarization on alternate laser shots. This procedure enabled the measurement of the total angular momentum orientation $\langle A_{10} \rangle$ and alignment $\langle A_{20} \rangle$ from ratios of the total signal intensities in the appropriate geometries.⁴⁹ These parameters are required in order to normalize the image intensities, as described fully elsewhere.⁴⁶ Circularly polarized probe laser radiation was generated using a photoelastic modulator, and in this case, geometries were switched from L to R circular polarization on alternating laser shots. Note that in switching from L to R circularly polarized probe radiation, only the sensitivity to the odd polarization moments (orientation) is changed. While circularly polarized light was used primarily to determine the angular momentum orientation, the geometries employed also contain information about alignment effects, and thus supplement the “normal” alignment geometries, and ensure a more stringent constraint on the data fitting.

Finally, images were also recorded on alternate pairs of shots with and without firing the photolysis laser. This procedure allowed the total signal and “probe-only” ion images to be accumulated concurrently and subsequently subtracted, if necessary, to remove background signal arising from ions formed through processes involving only the probe laser wavelength. In practice, the probe laser power could be attenuated sufficiently, using a variable neutral density filter that a “background subtraction” of the probe only signal from the pump-probe signal was found to be unnecessary.

B. Data analysis

The analysis of angular momentum polarization effects by fitting Fourier moments of the ion images^{40,42} has been described in detail previously.⁴⁶ The experimentally acquired images can be written in the form of a Fourier series,⁴⁶

$$\mathcal{I}(r, \Phi) = C_0(r) + 2 \sum_{n>0} C_n(r) \cos n\Phi + C'_n(r) \sin n\Phi, \quad (1)$$

where the Fourier moments, $C_n(r)$, can be obtained from appropriate integrals over the experimental images.⁴⁰ The Fourier moments are related to a set of dynamical functions, $f'_K(q, q'; v)$, which may be derived by fitting simulated Fourier moments of the images to the experimental data. The $f'_K(q, q'; v)$ terms contain the polarization information of interest for the system.⁵⁰ They are defined as^{46,49,50}

$$f'_K(q, q'; v) = \frac{f_K(q, q'; v)}{\langle f_0(0, 0; v) \rangle + 2 \langle f_0(1, 1; v) \rangle},$$

where $\langle f_K(q, q'; v) \rangle$ represent the integral of the dynamical functions over recoil speed. In the present work, the speed dependence of the dynamical parameters is expressed as a linear combination of Gaussian functions centered at a series of equally spaced speeds, v_i ,

$$f'_K(q, q'; v) = N \sum_{i=0}^{i_{\max}} a_K(q, q'; i) e^{-\sigma(v_i - v)^2}, \quad (2)$$

where N is a normalization constant, $a_K(q, q'; i)$ are Gaussian specific polarization parameters, σ is a width parameter, and v_i are the Gaussian centers. In practice, the $f'_K(q, q'; v)$ dynamical functions are usually recast in terms of a variety of different (but equivalent) factors, including the polarization parameters of Rakitzis and Zare⁵¹ and the polarization anisotropy parameters of Vasyutinskii and co-workers.^{49,52-54} For comparison with previous work, both sets are used here.

The best-fit coefficients $a_K(q, q'; i)$ for a given number of Gaussians, $i_{\max}=30$, were determined using a genetic algorithm which was selected from a pool of parameters randomly generated within the constraints of the physically allowed values. A Monte Carlo procedure, described fully elsewhere,⁴⁰ was then used to determine the errors on the fitted coefficients and on the speed dependent moments of the angular distribution. To reduce the number of fitting coefficients, the speed dependence of the polarization parameters was reexpressed in terms of a Legendre polynomial expansion.⁴⁶ The fitted coefficients for all polarization parameters from Eq. (2) [excluding those for the speed distribution, characterized by the set of coefficients $a_0(i) \equiv a_0(0, 0; i) + 2a_0(1, 1; i)$] were expressed as a convolution of the speed distribution parameters and a Legendre polynomial $[P_l(\cdots)]$ series with n_{leg} , the maximum order, set to 5,

$$a_K(q, q'; i) = a_0(i) \sum_{l=0}^{n_{\text{leg}}} b_K(q, q'; l) P_l(x_i), \quad (3)$$

where

$$x_i = 2 \frac{i-1}{i_{\max}-1} - 1. \quad (4)$$

This procedure allowed for the speed dependence of the polarization parameters, while significantly reducing the basis set size.

In the case of diatomic molecules, the dynamical functions have been interpreted in terms of contributions to the

dynamics by transitions to the dissociation continuum with their transition dipole moment vectors lying either parallel ($q, q'=0$) or perpendicular ($q, q'=\pm 1$) to the bond axis.⁵⁵ Interpretation of the polarization parameters in the case of larger systems^{54,56} is more problematic and awaits a detailed theoretical treatment. Here, as previously,^{42,43,46,57-59} we have used the polarization parameters to determine the molecular frame state multipoles, $\rho_{KQ}^{\text{mol}}(\theta; v)$, using the equations given elsewhere.^{46,49} These molecular frame parameters are functions of velocity and angle θ between the recoil direction and the electric vector of the photolysis light.

III. RESULTS

Although $\text{O}(^3P_2)$ fragments can, in theory, have nonzero high rank alignment ($K=4$) and orientation ($K=3$) parameters, the REMPI transition used is not sensitive to them (i.e., the linestrength factors, P_K , are zero).⁶⁰ In the case of photodissociation at 248 nm, up to eight pump-probe polariza-

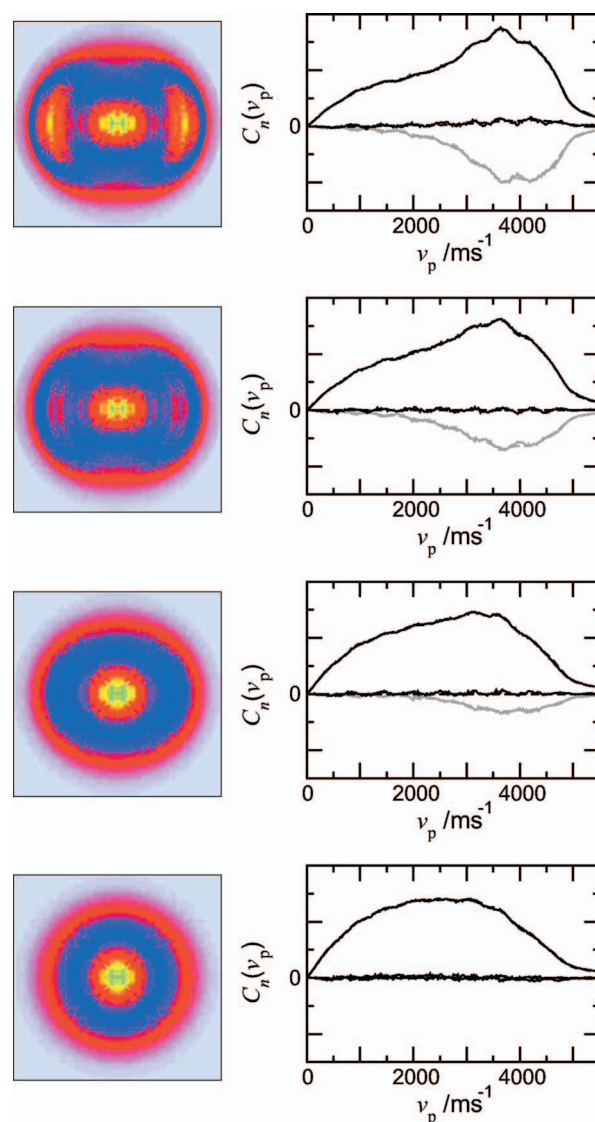


FIG. 2. (Color) Dissociation wavelength, 248 nm. Images, Fourier moments (—), and fits (---) for $\text{O}(^3P_1)$ products. Pump-probe geometries, from top to bottom: HH, HV, VH, and VV. Nonzero experimental and fitted C_2 moments are shown in gray.

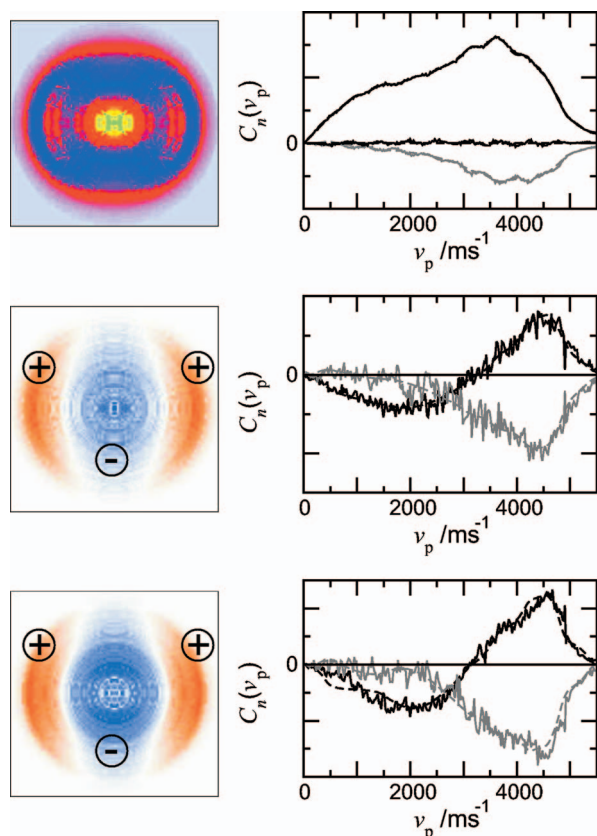


FIG. 3. (Color) Dissociation wavelength, 248 nm. Images, Fourier moments (—), and fits (---) for (top) $\text{O}(^3P_0)$ products in the HH pump-probe geometry, (middle) $\text{O}(^3P_1)$ products, and (bottom) $\text{O}(^3P_2)$ products dissociated with -45° polarized photolysis light. The last two images and Fourier moments shown are the differences between sets of data collected with left- and right-circularly polarized probe light. Positive and negative intensity portions of the images have been marked. Nonzero experimental and fitted C_2 moments are shown in gray. The spacing of the abscissa marks on the last two panels correspond to one-tenth of the spacing of the abscissa marks on the top panel.

tion combinations have been employed for $\text{O}(^3P_1)$ and $\text{O}(^3P_2)$ product detection to allow determination of all the polarization parameters. Note that for each spin-orbit state, all images were fitted simultaneously. A selection of images, extracted Fourier moments, and fits to the data are shown in Figs. 2 and 3. Using circularly polarized photolysis radiation allowed the probing of the in-plane orientation, characterized by the α_1 and γ_1 parameters. However, for both the $J=1$ and 2 fragments the difference between the RR and RL images was found to be zero within experimental error, indicating that α_1 and γ_1 are negligibly small. In contrast, the difference between -45°L and -45°R images, which is sensitive to the out-of-plane orientation parameter γ'_1 , was found to be significant for both the $\text{O}(^3P_1)$ and $\text{O}(^3P_2)$ products, as shown in Fig. 3. This figure also includes the HH image for the $\text{O}(^3P_0)$ products. As these products have no angular momentum, an image recorded in a single geometry is sufficient to recover all scalar and vector properties.

The one-color probe only images obtained at 226 nm were analyzed in the same way as the pump-probe images. However, the number of geometries that can be achieved in a one-color experiment is limited to HH, VV, and CC, where C represents either L or R circular polarization. This imposes

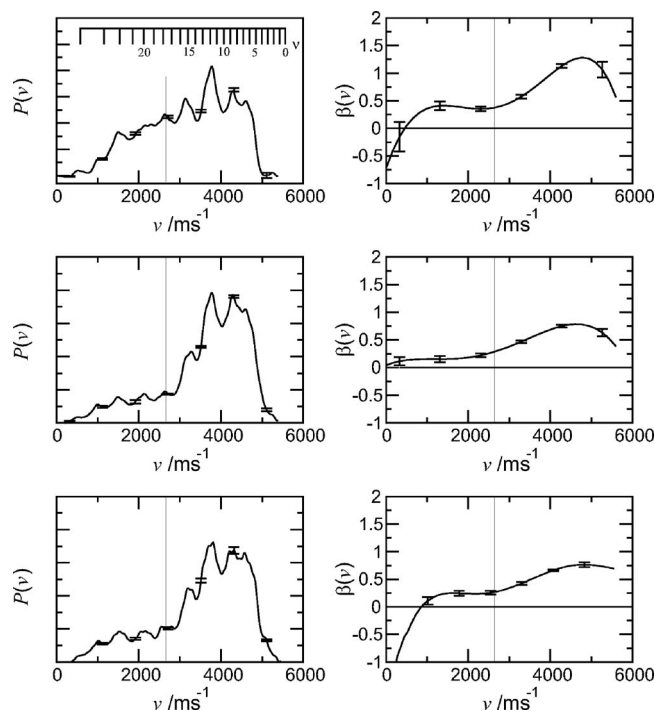


FIG. 4. Dissociation wavelength, 248 nm. Speed distributions and $\beta(v)$ parameters for (top to bottom) $\text{O}(^3P_2)$, $\text{O}(^3P_1)$, and $\text{O}(^3P_0)$. A comb for the vibrational state of $\text{O}_2(X^3\Sigma_g^-)$ in the absence of rotational excitation is shown in the top left panel. Errors represent a 1σ confidence limit. The separation between fast and slow regimes is marked with a vertical dotted line.

significant limitations on the number of dynamical parameters that can be extracted. In the present case, only speed distributions and spatial anisotropy parameters could be determined reliably, and all polarization parameters were artificially set to zero in the fitting process. Although this was found to have a negligible effect on the returned values of β , the overall quality of the fit was reduced, and thus the errors associated with the returned parameters increased accordingly. Note that for one-color studies, each spin-orbit state product was probed following photolysis at slightly different wavelengths, corresponding to the specific REMPI probe transitions (225.6, 226.0, and 226.1 nm for $\text{O}(^3P_2)$, $\text{O}(^3P_1)$, and $\text{O}(^3P_0)$ products, respectively⁶¹). These wavelengths are collectively referred to here as dissociation at 226 nm.

The speed distributions and spatial anisotropy parameters extracted from the data at the two dissociation wavelengths employed are shown in Figs. 4 and 5. At both wavelengths the speed distributions are bimodal and quite structured, in accordance with previous works.^{10–12,15,16,23} Marked in these figures is the approximate velocity which separates the fast and slow components of the bimodal distribution, as discussed in more detail in Sec. IV A. The data reported here for dissociation at 226 nm are either of higher resolution or form a more complete set than presented previously.^{11,12,14,17} The speed distributions for dissociation at 226 nm have been converted into a total kinetic energy distributions and are in excellent agreement with previous works for $\text{O}(^3P_2)$ and $\text{O}(^3P_1)$.^{17,23} The speed dependent polarization parameters obtained for dissociation at 248 nm are presented in Fig. 6, while speed averaged β and polarization

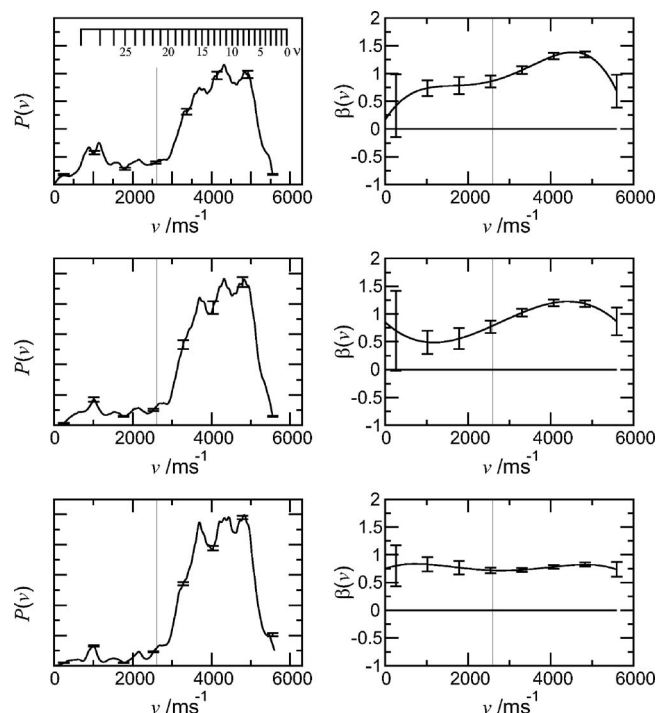


FIG. 5. Dissociation wavelength, 226 nm. Speed distributions and $\beta(v)$ parameters for (top to bottom) $O(^3P_2)$, $O(^3P_1)$, and $O(^3P_0)$. A comb for the vibrational state of $O_2(X^3\Sigma_g^-)$ in the absence of rotational excitation is shown in the top left panel. Errors represent a 1σ confidence limit. The separation between fast and slow regimes is marked with a vertical dotted line.

parameters are given in Table I. The data for dissociation at 248 nm represent the first complete characterization of the angular momentum polarization of $O(^3P_J)$ products from the dissociation of ozone.

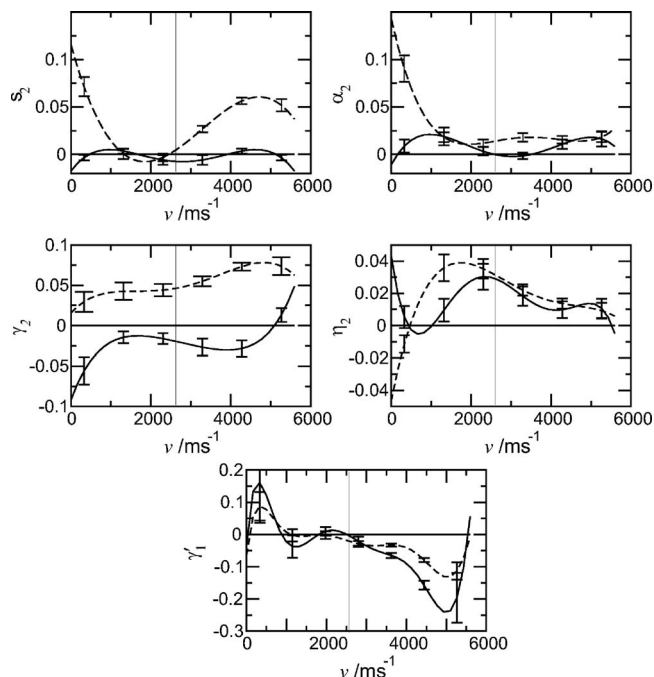


FIG. 6. Dissociation wavelength, 248 nm. Speed dependent angular momentum alignment and orientation parameters following dissociation at 248 nm for $O(^3P_2)$ (—) and $O(^3P_1)$ (---). All parameters not displayed here were found to be zero within experimental confidence limits. Error bars indicate 1σ confidence limit. The separation between fast and slow regimes is marked with a vertical dotted line.

TABLE I. Speed averaged spatial anisotropy and polarization parameters for $O(^3P_J)$ fragments following dissociation at 248 and 226 nm. 1σ errors reported refer to the last digit(s) shown. γ_1 and α_1 orientation parameters were found to be zero at 248 nm. The limiting values for the polarization parameters have been given in Ref. 76, with those for the alignment moments reproduced in Ref. 41. The measured values of the parameters are typically at least five to ten times smaller than the limiting values.

| | $O(^3P_2)$ | $O(^3P_1)$ | $O(^3P_0)$ |
|-------------|------------|------------|------------|
| 248 nm | | | |
| β | 0.73(2) | 0.55(2) | 0.53(2) |
| γ'_1 | -0.073(4) | -0.050(2) | |
| s_2 | -0.002(2) | 0.038(2) | |
| α_2 | 0.007(3) | 0.018(3) | |
| γ_2 | -0.020(6) | 0.063(5) | |
| η_2 | 0.016(4) | 0.019(3) | |
| 226 nm | | | |
| β | 1.14(6) | 1.08(6) | 0.78(2) |

IV. DISCUSSION

A. Speed distributions and β parameters

As noted in Sec. I, the diffuse structure observed in the speed and kinetic energy release distributions has been demonstrated previously to be due to vibrational excitation of the $O_2(X^3\Sigma_g^-)$ cofragment.^{10,17} We have therefore simulated the O_2 cofragment internal energy distributions in an attempt to recover spin-orbit state specific O_2 coproduct vibrational state populations. An example of simulation is shown in Fig. 7. In these simulations, the vibrational state distributions were optimized, while the rotational state populations were fixed to Gaussian functions peaking at $J_{O_2}=40$ with a full width at half maximum of 15. These estimates represent an

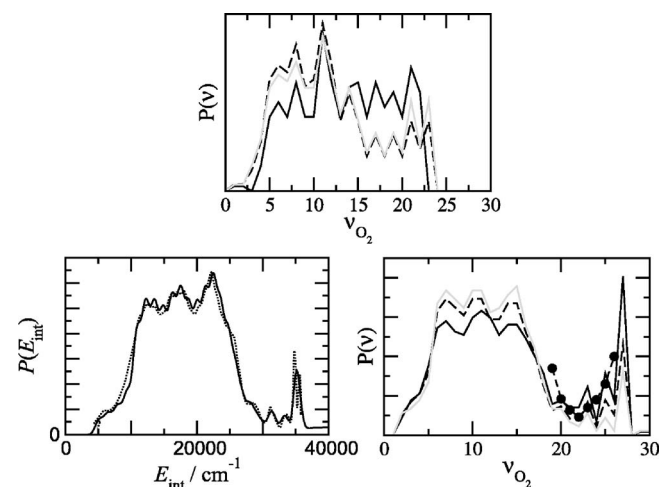


FIG. 7. Bottom left: Example raw data (····) and fit (—) to the internal energy distribution of the O_2 cofragments of $O(^3P_0)$ generated from the photodissociation of ozone at 226 nm. Refer to text for details of the simulations. Top panel: $O_2(X^3\Sigma_g^-)$ vibrational state populations recovered from fits to the speed distributions for dissociation at 248 nm for $O(^3P_2)$ (—), $O(^3P_1)$ (---), and $O(^3P_0)$ (gray solid line). Bottom right panel: As for the top panel but for dissociation at 226 nm. In all fits, the rotational distributions were modeled using a Gaussian function peaking at $J=40$ with a width of 15 units of angular momentum.²⁵ Average errors of around 25% are associated with the reported populations. Vibrational populations from the work of Miller *et al.* (Ref. 10) are shown in the bottom right panel as filled circles.

approximate average from the vibrationally state-resolved rotational distributions reported by Daniels and Wiesenfeld following dissociation at 248 nm.²⁵ The results of these simulations are shown in Fig. 7. The data at 226 nm are compared with the vibrational state distribution measured by Miller *et al.*¹⁰ in the bottom right panel of the figure, where the agreement is seen to be very good. The distribution of Miller *et al.*, which was determined by LIF of O₂, was insensitive to the spin-orbit state of the atomic coproduct and should therefore be compared with a weighted average of the distributions recovered from the present study. The present populations also compare well with the LIF results obtained by Park and Slanger at 248 nm.²⁴ Our distributions agree best with the LIF data obtained via the $B(v'=0)$ excited state, which were thought by Park and Slanger to be in error but less well with those obtained via the $B(v'=2)$ intermediate state, which were thought to be correct.²⁴ However, even in the latter case, the vibrational distributions extracted here capture well the principal feature given in the work of Park and Slanger.²⁴ Increasing the mean rotational excitation to $J_{O_2}=59$, closer to the value observed in the calculations of Qu *et al.*,²⁹ results in a somewhat colder vibrational distribution for the fast fragments, in slightly better agreement with the vibrational distribution measured by Park and Slanger at 248 nm.²⁴

For the fast products, which account for the majority of O(³P_{*J*}) atoms, the distributions are largely independent of the spin-orbit state, indicating *diabatic* behavior with respect to the spin-orbit coupling interaction at long range. This is supported by the near statistical spin-orbit populations reported at wavelengths between 226 and 266 nm.^{10–12,15,17,23} In contrast with the behavior of the fast fragments, the intensity of the slow products, corresponding to O(³P_{*J*}) atoms born in partnership with highly vibrationally excited O₂($X^3\Sigma_g^-$), varies significantly with spin-orbit state. The spin-orbit populations for the slow fragments can be estimated using the speed averaged values from the literature (see Ref. 17 and references therein): We have assumed these total spin-orbit populations to be statistical over the wavelength region of interest. With this assumption, at 248 nm, the population ratio for the slow products only is O(³P₂):O(³P₁):O(³P₀)=7:3:1. At 226 nm they are even more markedly non-statistical, with O(³P₂):O(³P₁):O(³P₀)=17:5:1. In light of the Massey criterion,⁶² it seems reasonable to suppose that the slow fragments behave more adiabatically in the spin-orbit recoupling zone than the fast fragments. If that is the case, the finding of a preferential population (above the statistical value) in $J=2$ raises questions about which surface(s) is(are) responsible for production of the slow fragments, as discussed further below. Note that the conclusion that the slow fragments cannot be treated diabatically is reinforced by the fact that there are significant differences in the speed distributions for the three spin-orbit components below around 2600 m s⁻¹, suggesting that slow-moving O atoms in different spin-orbit states are partnered by O₂ cofragments in different rovibrational states. Similar differences have been commented on previously by Geiser *et al.* at different wavelengths across the Hartley band.¹⁷

An adiabatic, Ω -conserving correlation diagram for dis-

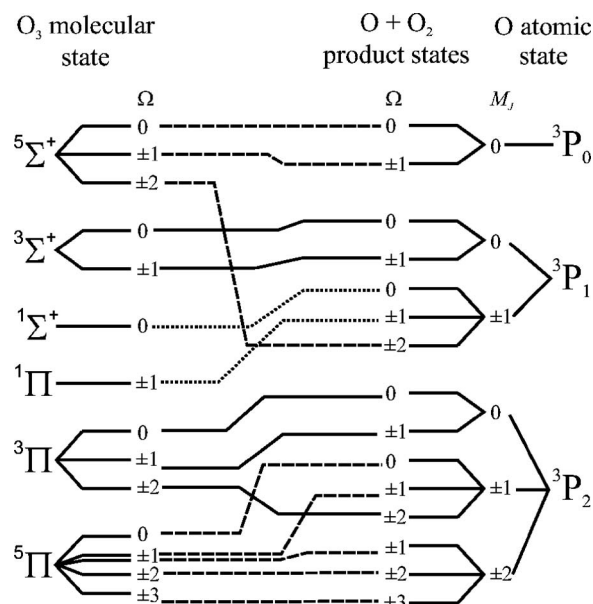


FIG. 8. Adiabatic, Ω -conserving correlation diagram for dissociation of ozone to ground state products at linearity. The ordering of the molecular states is taken from the work of Rosmus *et al.* (Ref. 36). The energy ordering of the M_J states and of the Ω states has been established on the basis of Hund's rules. Different line styles have been used to facilitate the reading of the correlations. The $^5\Pi$ molecular state has $\Omega \pm 1$ components, which arise from different combinations of the projections of the spin quantum numbers from atomic and molecular entities.

sociation of ozone to ground state products at linearity is shown in Fig. 8. It is complicated in the long-range region by the convergence of states of singlet, triplet, and quintet symmetries to the ground state asymptote. The relevant singlet electronic states of ozone in the long-range region are discussed in more detail in Sec. IV B 2. From this diagram, it is evident that adiabatic, Ω -conserving dissociation at linearity on either the $^1\Sigma(\tilde{R})$ state or on the ground state $^1\Pi(\tilde{X})$ state would only result in formation of O(³P₁) products. Furthermore, a fully adiabatic correlation, i.e., one in which Ω is not conserved, would lead to the same conclusions. This finding is at variance with the experimental measurements. However, it is important to consider the adiabatic correlation of states at geometries away from linearity. On bending to angles smaller than $\sim 160^\circ$, the *ab initio* calculations by Rosmus *et al.*³⁶ and Tashiro and Schinke³⁷ indicate that the relative ordering of singlet, triplet, and quintet states changes. The $1^1A'(^1\Pi)$ state becomes the overall lowest in energy, while the $2^1A'(^1\Sigma)$ is the highest (see the inset of in Fig. 1). Although we have not constructed the full adiabatic correlation diagram for nonlinear geometries, based on the relative ordering of the states in C_s symmetry,^{36,37} it is evident that adiabatic dissociation on the ground $\tilde{X}(1^1A')$ electronic state would be expected to lead to the sole formation of O(³P₂) products, while adiabatic dissociation on the $\tilde{R}(2^1A')$ state would lead to O(³P₀) products. Given the relatively large energy separation between the $\tilde{X}(1^1A')$ and $\tilde{R}(2^1A')$ states, even at quite large separations,^{36,37} it is also hard to see how dissociation on the *excited*, repulsive \tilde{R} state surface could give rise to preferential population in the *lowest* $J=2$ spin-orbit state of the atomic products. Although the strong popu-

TABLE II. Spatial anisotropy parameters averaged over fast and slow speed regimes for $O(^3P_2)$ fragments at a series of wavelengths. The fraction of slow products formed is also given.

| | 266 nm ^a | 248 nm | 240 nm ^a | 230 nm ^a | 226 nm | 226 nm ^a |
|-----------|---------------------|---------|---------------------|---------------------|---------|---------------------|
| $N(v_i)$ | 0.25 | 0.25(2) | 0.19 | 0.20 | 0.18(2) | 0.17 |
| β_f | 0.71(15) | 0.79(3) | 1.10(30) | 1.52(30) | 1.29(6) | 1.31(20) |
| β_s | ... | 0.37(2) | 0.56(7) | 0.80(7) | 0.59(4) | 0.67(5) |

^aValues calculated from the kinetic energy release distributions published in the works of Wilson and co-workers (Refs. 14 and 17), assuming a cutoff between fast and slow fragments at a total kinetic energy of 0.84 eV. Where given, errors represent a 1σ confidence limit.

lation propensities indicated by the adiabatic model are not fully consistent with experiment, adiabatic dissociation on the ground state of ozone would be expected to yield the observed bias in population toward the lowest spin-orbit state, particularly if one allows for dissociation from a range of bending coordinates. We note that similar arguments have been used to explain the origin of slow-moving $S(^3P_J)$ products in the photodissociation of OCS.⁵⁹ Theoretical studies of the reverse of the dissociation process discussed here, namely, the recombination of $O(^3P_J) + O_2(X^3\Sigma_g^-)$ to form the O_3 complex, are also worth recalling.³⁷ Although the recombination process is far from being completely understood,⁶³ Tashiro and Schinke found that the spin-orbit coupling played a relatively minor role at thermal energies, and that an adiabatic treatment of the recombination led to relatively minor errors in the thermal rate coefficient.³⁷ The energies involved in the collisional study are only slightly smaller than those sampled by $O(^3P_J)$ born in conjunction with the most highly vibrationally excited $O_2(X^3\Sigma_g^-)$ cofragments of interest here.

Because the \tilde{B} state has no identified accessible crossings with the ground state (see, for example, the work of Qu *et al.*³⁵), population of the latter following optical excitation into the Hartley band is likely to occur *via a series of curve crossings* involving at least one intermediate state. A possible contender for this intermediate state is the \tilde{A} state. A seam of conical intersection has been identified between the \tilde{A} state and the \tilde{X} state.^{64–68} The conical intersection, which is located at coordinates near the energy minimum of the \tilde{A} state,⁶⁴ could therefore constitute a gateway to the ground electronic state for products that have previously crossed from the \tilde{B} to the \tilde{A} state.⁶⁸

Another interesting aspect of the speed distributions reported here at both 226 and 248 nm is the speed that separates the fast and slow fragments. This is found to be around 2600 m s^{-1} , corresponding to a kinetic energy release of $E_{\text{kin}} \sim 0.84 \text{ eV}$. This value is close to that is also evident in the kinetic energy release distributions presented by Houston and co-workers at a number of wavelengths across the Hartley band.^{10,17} This suggests that a crossing between the diabatic surfaces is available only to those products that are generated below a certain threshold speed and, hence, above a certain level of O_2 vibrational excitation. It is proposed that these fragments correlate with highly vibrationally excited parent molecules on the \tilde{B} state surface. This is consistent with a Landau-Zener picture of the dynamics, such as the

one used by Qu *et al.* to model the \tilde{B}/\tilde{R} crossing.²⁹ In that case, the authors expressed the “hopping” probability P as a function of the energy separation of the *adiabatic* potentials ΔE at the point where the diabatic states cross and the time spent in the interaction region τ ,

$$P = 1 - e^{-\xi\pi\Delta E\tau/2},$$

where the parameter ξ was adjusted to reproduce the quantum yield of triplet products.²⁹ The interaction time τ is related to the ratio of the range of the interaction zone d and the velocity of the system perpendicular to the crossing seam v_{\perp} . According to this equation, a very small energy separation between the adiabatic states involved is needed to explain the low velocity selectivity of the \tilde{B}/\tilde{A} crossing. Balvitcha and Balint-Kurti⁶⁹ have recently singled out the seam between the diabatic \tilde{B} and \tilde{A} states as corresponding, in the adiabatic representation, to states with extremely small energy separations. Coupled with evidence discussed above, it is proposed that the seam sampled by the slow fragments is the \tilde{B}/\tilde{A} seam. According to the Landau-Zener picture of the triplet dissociation dynamics,²⁹ the large energy splitting between the adiabatic states renders the \tilde{B} to \tilde{R} crossing accessible to fragments with relatively large velocities perpendicular to the seam. The \tilde{B}/\tilde{A} crossing, on the other hand, is only accessed by molecules with large vibrational excitation, which results in small perpendicular velocities at the crossing seam.

The possibility that the \tilde{B}/\tilde{A} surface crossing plays a role, and is only accessible to the most highly vibrationally excited molecules, is consistent with the wavelength dependence of the population of slow fragments that can be established by comparing the studies presented here with those of Houston and co-workers.^{10,17} The fractions of slow products generated at five different wavelengths within the Hartley band are compared in Table II. The numbers from Geiser *et al.* have been estimated from their published kinetic energy release distributions,¹⁷ assuming a cutoff between fast and slow fragments at $E_{\text{kin}} \sim 0.8 \text{ eV}$. With the exception of the data at 240 nm,¹⁷ a steady increase in the population of the slow channel with decreasing excitation energy is observed, which corresponds to lower kinetic energies. Geiser *et al.*¹⁷ have pointed out that the population specifically in $v_{O_2} \geq 26$ increases with *increasing* excitation energy, the opposite trend to that of the overall population of the slow component of the bimodal velocity distribution discussed here. As noted in Sec. I, Houston and co-workers invoked the participation

of triplet states to explain the presence of the slow component at excitation wavelengths as long as 266 nm (see further below). The proposal in the present work is that the process that makes $v_{O_2} \geq 26$ and the process leading to the slow component of the velocity distribution, with v_{O_2} in the range of ~ 15 –26, are, in fact, one and the same and reflect the geometries of the \tilde{B} to \tilde{A} crossing seam. According to the above picture, there are two factors at play in determining the probability of crossing from the \tilde{B} to the \tilde{A} surface. The first is that molecules must spend a sufficient time in the crossing region, i.e., they must have small perpendicular velocities v_{\perp} . This requires high ozone internal excitation, which correlates to high O_2 photofragment vibrational excitation or, alternatively, lower photon energies. Secondly, trajectories must also have sufficient total energy to be able to access the crossing region. The suggestion is, therefore, that the combined effects of these two constraints account for the dynamical threshold for production of $v_{O_2} \geq 26$, which favors their formation at shorter wavelengths.¹⁷

Calculations by Baloitcha and Balint-Kurti⁶⁹ and Qu *et al.*⁷⁰ indicate that the equilibrium O–O bond length is 20% greater on the \tilde{A} state than on the \tilde{B} state, thus providing a further rationale for the vibrational excitation of the O_2 cofragment. The bending potentials of Qu *et al.*⁷⁰ also help us to shed light on the rotational excitation of the highly vibrationally excited O_2 cofragments. They indicate that the product flux, once transferred to the \tilde{A} state, should undergo a bond closing motion, tending toward the D_{3h} well, which is located close to the conical intersection with the ground state. Once the flux has funneled through the conical intersection, it will tend back toward the ground equilibrium bond angle, found at 117° , experiencing a torque contrary to that imposed on the \tilde{A} state and also counteracting that imparted on the departing $O_2(X^3\Sigma_g^-)$ fragments by the impulse associated with bond breaking. The torques generated on these surfaces are likely to affect the rotational energy of the highly vibrationally excited $O_2(X^3\Sigma_g^-)$ products. From Fig. 7, which is representative of the fits obtained, it is evident that while a fixed rotational distribution provides a reasonable model of the fast fragments, the width of the peaks corresponding to the slow product envelope is less well reproduced. Indeed, a better match in this energy region may be obtained by using a rotational distribution that peaks at $J_{O_2}=10$, with a width of $\Delta J_{O_2}=5$. This indicates that the rotational energy distributions for the highest vibrational states are considerably narrower than for O_2 in lower vibrational states. This result is consistent with the dynamics described above, in which the impulse associated with bond breaking is counteracted by the torque experienced by products dissociating *via the ground electronic state*.

The spatial anisotropy parameters in the present work are in excellent agreement with the results of Wilson *et al.*¹⁴ (see Table II). At high velocities, the values of β are similar to those reported for the singlet channel dissociation within the Hartley band, i.e., in the region of $\beta=1.0$ –1.4 (see Figs. 4 and 5). Following Wilson *et al.*,¹⁴ these high speed values can be interpreted in terms of prompt dissociation from bond angles close to the equilibrium value. At lower recoil veloci-

ties, β drops to approximately 0.5, remaining constant at this value for most of the slow products. Wilson *et al.* have interpreted this behavior as an indication of the operation of a bond closing mechanism prior to dissociation,¹⁴ with bond angles of around 90° needed to explain the observed reduction in β . This explanation might seem somewhat at odds with the rotational energy release deduced for slow fragments and with the mechanism proposed above for their production. A further cause for a reduction of the β parameter from the Hartley band value may be nonaxial recoil. However, this possibility seems unlikely, given that the slow products have been found to possess relatively low levels of rotational excitation.²⁵ A reduction in β might also reflect, in addition to bond closure, the influence of parent molecule rotation on the timescale of dissociation. While the dissociation lifetime for direct dissociation on the diabatic \tilde{B} state, leading to singlet products, is known to be of the order of only 50 fs,²⁷ it is possible that the flux undergoing highly vibrationally excited motion, and sampling multiple surface crossings before dissociating on the ground state, may have a considerably longer associated lifetime. If lifetime effects do play a role in reducing β , it is interesting that extensive vibrational energy redistribution does not also take place. This might indicate that the system evolves quickly after the final vibrational excitation of the O_2 moiety has been established, which may be either at the \tilde{B}/\tilde{A} crossing or the \tilde{A}/\tilde{X} conical intersection. Trapping of part of the wavefunction on the \tilde{B} state, in particular, prior to crossing to the \tilde{A} state is plausible, given the observation of trapped trajectories,^{27,30–34} and the structured autocorrelation function^{27,71} and absorption spectrum.^{27,68,69,71,72} Perhaps coincidentally, the relative amplitudes of the long-time features in the experimental autocorrelation functions⁷¹ are of a similar order of magnitude as the yield of highly vibrationally excited O_2 products. Trapping of a highly vibrationally excited wavepacket on the \tilde{B} state surface might also enhance the total crossing probability to the \tilde{A} state, which would otherwise be inaccessible to those molecules undergoing prompt, direct dissociation on the \tilde{B} state. In summary, it seems probable that both bond closure and lifetime effects play some role in the reduction of β from the value taken in the singlet product channel of the Hartley band.

Several alternative mechanisms for generating slow products in coincidence with highly vibrationally excited O_2 products should also be considered briefly. Products may access the ground state following direct excitation to the \tilde{A} state. This possibility seems improbable on account of the oscillator strength for this state, which has been calculated by Palmer and Nelson to be over 10^5 times smaller than for excitation into the \tilde{B} state.⁷³ Another possibility is that the product flux on the \tilde{A} state may lead to triplet products by crossing onto the \tilde{R} state. This crossing has not been characterized, so it is difficult to make a definitive judgement on the likelihood of this mechanism. However, in this case the torque experienced by the system on the \tilde{A} state does not counteract the impulse from the breaking bond, and relatively high rotational excitation of the molecular cofragment

TABLE III. $O(^3P_J)$ atomic angular momentum polarization parameters for the fast and slow photofragments subsequent to dissociation at 248 nm. 1σ errors reported refer to the last digit(s) shown. The limiting values for the polarization parameters have been given in Ref. 76, with those for the alignment moments reproduced in Ref. 41. The measured values of the parameters are typically at least five to ten times smaller than the limiting values.

| | $O(^3P_2)$ | | $O(^3P_1)$ | |
|-------------|------------|-----------|------------|-----------|
| | Slow | Fast | Slow | Fast |
| β | 0.37(2) | 0.79(3) | 0.15(1) | 0.60(3) |
| γ'_1 | -0.009(2) | -0.086(5) | 0.007(2) | -0.059(3) |
| s_2 | 0.001(2) | -0.002(2) | 0.005(3) | 0.041(3) |
| α_2 | 0.015(6) | 0.006(3) | 0.023(4) | 0.016(3) |
| γ_2 | -0.016(5) | -0.021(6) | 0.042(4) | 0.065(5) |
| η_2 | 0.015(4) | 0.016(4) | 0.032(6) | 0.018(3) |

might be expected, in contrast with the present findings. Furthermore, as discussed above, this mechanism is not expected to yield spin-orbit state populations for the slow products in agreement with experiment. Finally, it is also important to consider the possibility of triplet (or quintet) states being involved in the production ground state products, as suggested by Geiser *et al.*¹⁷ Given the complex manifold of molecular electronic states of ozone, it is not possible to discount their involvement. However, it is worth noting that all except one of the ten or so triplet states that cross the \tilde{B} and \tilde{R} state surfaces actually correlate to spin forbidden products.⁷⁴ The one exception, the $2^3A'$ state, follows closely the energy of the \tilde{R} state⁷⁴ and correlates adiabatically with either $O(^3P_0)$ or $O(^3P_1)$ products.³⁷ It is therefore unlikely to be involved in the production of the slow $O(^3P_J)$ products, which we find are preferentially populated in $J=2$. Two other triplet states, the $1^3A'$ and $1^3A''$ states, which play a role in the Wulf bands,²⁷ also correlate with ground state products, this time with $O(^3P_2)$.³⁷ However, in the Franck-Condon region, these states lie relatively low in energy, and their participation in the dynamics subsequent to excitation into the Hartley band seems unlikely.

B. Angular momentum alignment

The above discussion of the speed distributions and spatial anisotropy parameters suggests that fast and slow fragments follow considerably different dissociation pathways. As a result, the angular momentum polarization data have also been divided into fast and slow channels. The associated polarization parameters are given in Table III. From these data, the molecular frame J -state multipoles $\rho_{KQ}(J)$ and M_J state populations have been calculated,^{46,49} and are presented in Figs. 9 and 10, respectively. The $O(^3P_2)$ products exhibit very little alignment, as demonstrated by their near-isotropic M_J populations at both high and low velocities. On the other hand, $O(^3P_1)$ products exhibit alignment of \mathbf{J} preferentially along the recoil direction, resulting in positive values of $\rho_{20}(J)$ and preferential population in $M_J = \pm 1$. The behavior of slow and fast products is similar, although in the former case, the polarization is significantly less marked.

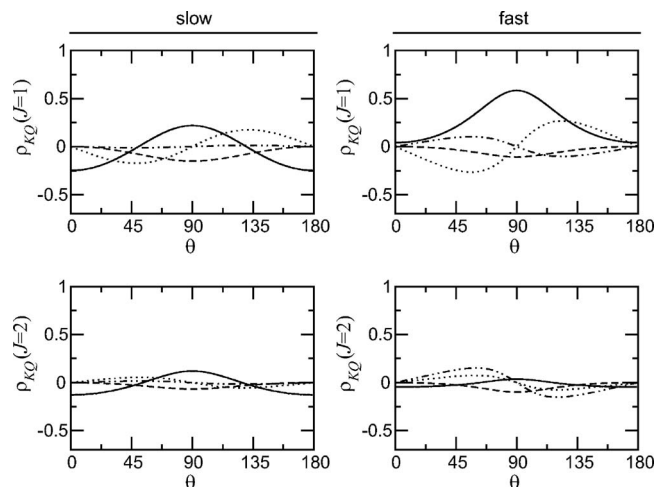


FIG. 9. Dissociation wavelength, 248 nm. Molecular frame J -state multipoles for slow and fast $O(^3P_1)$ and $O(^3P_2)$ fragments calculated using the equations in Sec. II B. Symbols represent $\text{Im}[\rho_{11}(J)]$ (---), $\rho_{20}(J)$ (—), $\rho_{21}(J)$ (---), and $\rho_{22}(J)$ (-·-·-). Maximum errors of approximately 50% are associated with state multipoles for $O(^3P_2)$ products, while a maximum of 15% with $O(^3P_1)$ multipoles.

1. The fast dissociation models

The presence of electron spin complicates the interpretation of the angular momentum polarization, and in the case of polyatomic systems, one is often forced to have recourse to a number of simplified limiting models.^{41,43,57,59} One of these, which is appropriate in the case of fast dissociation, treats the spin-orbit recoupling zone in a diabatic fashion.^{41,43} This allows the L - and S -state multipoles to be computed directly from the $\rho_{KQ}(J)$ presented above. A number of reasons can be presented in favor of a diabatic, as opposed to an adiabatic, treatment of the triplet dissociation of ozone leading to fast products. An adiabatic representation of the dissociation would predict nonstatistical spin-orbit populations, contrary to the experimental observations for the major fast product channel.^{10-12,15,17,23} Furthermore, the relative speeds

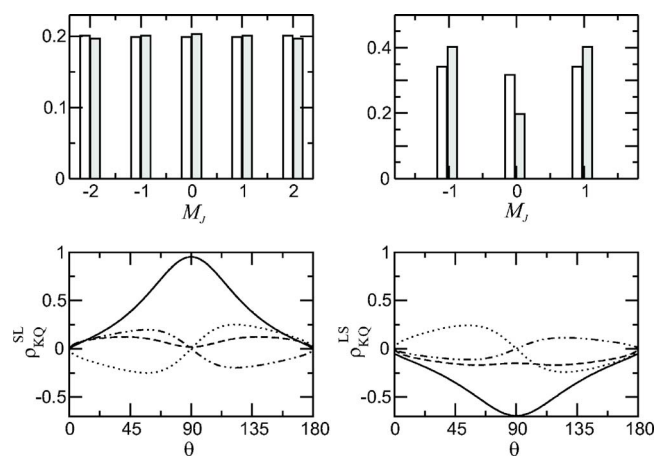


FIG. 10. Dissociation wavelength, 248 nm. Top panels: Scattering angle averaged M_J populations for $O(^3P_2)$ (left) and $O(^3P_1)$ (right) products. Populations corresponding to slow (white) and fast (gray) products have been plotted separately. Bottom panels: Molecular frame L/S -state multipoles for fast fragments calculated using the spin-polarized fast dissociation model. See text for details. Symbols represent $\text{Im}[\rho_{11}(J)]$ (---), $\rho_{20}(J)$ (—), $\rho_{21}(J)$ (---), and $\rho_{22}(J)$ (-·-·-).

of the fast products are high, and the fast dissociation model has been successfully applied to systems with similar⁴¹ or even smaller⁴³ relative velocities. Finally, the speed distributions and β parameters for the fast channel presented for the three spin-orbit states are very similar. In a diabatic picture, the speed distribution and β parameters for all spin-orbit states would be the same.

For these same reasons, it seems inappropriate to apply the fast dissociation model to the slow fragments. Their polarization is discussed in Sec. IV B 3.

Two types of fast dissociation model have been outlined previously: One in which the spin angular momentum is assumed to be unpolarized prior to reaching the recoupling zone,^{41,57} and the other in which allowance is made for the polarization of S .^{43,46,57} The spin-unpolarized model predicts that the $O(^3P_1)$ J -state multipoles of rank $K=2$ should be of similar magnitude but of the opposite sign to those for the $O(^3P_2)$ products.⁴¹ Inspection of the J -state multipoles shown in Fig. 9 clearly indicates that the spin-unpolarized model cannot be applied to this system. The spin-polarized model^{43,46,57} was therefore employed to estimate the L - and S -state multipoles by fitting the angle-dependent $\rho_{KQ}(J)$ multipoles for fast fragments displayed in Fig. 9. Unlike our previous work,^{41,43} orientation moments were also included in the fit to the experimental J -state multipoles, although in practice, fitting with the $K=1$ multipoles yielded very similar results to those obtained with the $K=1$ moments neglected. The L - and S -state multipoles returned by the analysis are shown in Fig. 10, where they have been labeled as $\rho_{KQ}(L/S)$ and $\rho_{KQ}(S/L)$ since the model does not identify which set are associated with the L and which with S . Possible assignment of the fitted state multipoles to L and S is made in Sec. IV B 2, by comparison with the predictions from a long-range interaction model of the L -state multipoles. However, irrespective of this assignment, the results of the spin-polarized model indicate that both orbital and spin angular momenta are polarized, one along the z axis (taken as the recoil direction⁴¹), characterized by a positive $\rho_{20}(L/S)$, and the other in the xy plane, characterized by a negative $\rho_{20}(S/L)$.

The predicted spin polarization warrants some discussion. Spin polarization has also been suggested by this model in the case of the $O(^3P_J)$ fragments from the photodissociation of SO_2 at 193 nm.⁴³ Brouard *et al.*⁴³ proposed that the spin polarization in the dissociation of SO_2 may be due either to the participation of triplet states prior to transition through the spin-recoupling zone or to a breakdown of the fast-recoil approximation itself. For the present system, the relative velocity for the fast products, i.e., those born in low vibrational states, is around 7500 m s^{-1} , leading to a Massey parameter nearly three times smaller than that for the O-atom fragments from the photodissociation of SO_2 at 193 nm. Under these conditions it seems more likely that the spin polarization is established before the recoupling zone, consistent with the participation of or mixing with triplet and quintet states during dissociation. As noted in Sec. IV A, the calculations by Rosmus *et al.* show that for comparatively modest bond extensions, around $R \sim 2.6 \text{ \AA}$, states of singlet, triplet, and quintet multiplicities not only become close in energy

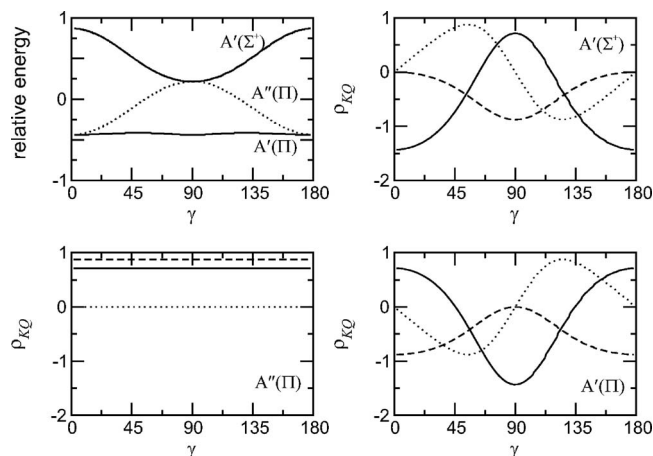


FIG. 11. Long-range interaction potentials and predicted state multipoles. See text for details. Symbols represent ρ_{20} (—), ρ_{21} (···), and ρ_{22} (---).

but also undergo curve crossings as a function of bond angle,³⁶ leading to significant spin contamination of the “singlet” wavefunctions in the region of the crossings. It seems that a more complete analysis of the dynamics would need to include the effect of these surfaces and their interactions.

2. The long-range interaction model

The L -state multipoles calculated using the fast dissociation model contain information about the surface(s) on which the system dissociates to generate triplet products. In the following, we use a long-range model of the potential energy surfaces, detailed previously,^{41,43,46,57,58,75} to help us determine which electronic states might be accessed during dissociation. The long-range potentials were calculated as described previously by diagonalizing the quadrupole-quadrupole electrostatic interaction matrix.^{46,75} The results of the diagonalization, alongside the predicted $\rho_{KQ}(\gamma)$ for products dissociating on each surface, are shown in Fig. 11. The ordering of the states was assigned on the basis of the *ab initio* calculations of Rosmus *et al.*³⁶ and the signs of the quadrupole moments of $O(^3P_J)$ and $O_2(X^3\Sigma_g^-)$. In the following, only the singlet states of ozone are considered in detail.

As noted in Sec. IV A, three singlet states converge on the $O(^3P_J)+O_2(X^3\Sigma_g^-)$ asymptote. The lowest energy state is of A' symmetry and correlates with the $X^1A'(^1\Pi)$ state at short range. Higher in energy lies the $1^1A''(^1\Pi)$ state, which at linearity is degenerate with the \tilde{X} state. The highest state is of A' symmetry, Σ^+ at linearity, and corresponds to the \tilde{R} state at short separations. The two states of A' symmetry interact strongly at $\gamma=90^\circ$, where the behavior of the surfaces is characteristic of an avoided crossing. The predicted $\rho_{KQ}(\gamma)$ multipoles may be compared with the experimentally determined L - and S -state multipoles presented in Fig. 10. The scattering angle averaged values of the experimental $\rho_{KQ}(L/S)$ and $\rho_{KQ}(S/L)$ moments are also given in Table IV. Note that ρ_{21} parameters average to zero over scattering angle.

Firstly, the assignment of state multipoles to L or S is attempted. Both $\rho_{20}(S/L)$ and $\rho_{22}(S/L)$ state multipoles in

TABLE IV. Scattering angle averaged orbital/spin angular momentum state multipoles computed using the spin-polarized fast dissociation model. Errors represent a 1 σ confidence limit.

| | ρ_{20} | ρ_{22} |
|-------|-------------|-------------|
| L/S | -0.48(6) | -0.15(4) |
| S/L | 0.57(7) | 0.09(3) |

Table IV are positive. In terms of the long-range interaction model, only dissociation on the $^1A''(^1\Pi)$ state would give rise to orbital angular momentum polarization similar to that reported here. Given the accepted dissociation mechanism described in the Introduction, it seems unlikely that $\rho_{20}(S/L)$ can be assigned to the L -state multipoles, and these are therefore believed to be associated with the spin angular momentum vector. Hence, the $\rho_{KQ}(L/S)$ multipoles are assigned to the polarization of the orbital angular momentum L . The $\rho_{20}(L/S)$ and $\rho_{22}(L/S)$ multipoles are both negative, and a suitable match to these data is found for products dissociating either on the $^1A'(^1\Sigma^+)$ surface sampling Jacobi angles $\gamma < 60^\circ$ or on the $^1A'(^1\Pi)$ surface at angles around $\gamma = 90^\circ$. Therefore, the polarization of the fast $O(^3P_J)$ atomic products presented here is consistent with dissociation on the $\tilde{R}(^1A'/^1\Sigma^+)$ surface at long-range, sampling Jacobi angles that correspond quite closely with the equilibrium bond angle of ozone. The rather narrow range of Jacobi angles suggested by the model is consistent with the value of β reported for these fragments. However, a more rigorous calculation of the polarization of the fast atomic fragments would require a full dynamical treatment of the dissociation that at least takes into account the averaging over Jacobi angles.

3. Slow fragments

In Sec. IV A, it was argued that the spin-orbit populations of the fragments born with low velocities might indicate near-adiabatic dynamics on the electronic ground state. The correlation arguments employed in that section can also be used to make predictions about the angular momentum polarization, which can be compared with the near-isotropic angular momentum distributions observed experimentally for the slow $O(^3P_1)$ and $O(^3P_2)$ fragments (see Fig. 10). From the correlation diagram for dissociation at linearity shown in Fig. 8, it is clear that the adiabatic dissociation on the ground $\tilde{X}(^1\Pi)$ state would lead to exclusive population of $M_J = \pm 1$ states of the $O(^3P_1)$ products. For bent geometries, dissociation on the ground state should correlate with $O(^3P_2)$ fragments strongly polarized along the quantization axis (i.e., with population of $M_J = \pm 2$ only). These propensities are much stronger than observed experimentally for the slow products. As noted in Sec. IV A, at nonlinear configurations, the adiabatic correlation for the \tilde{R} state would be expected to generate fragments exclusively in $J=0$, which cannot be polarized. This further points against the possibility that slow fragments emerging on the \tilde{R} state, via a crossing from the \tilde{A} state. It seems likely that the lack of angular momentum polarization for the slow fragments reflects partially the adia-

batic dissociation on the ground state surface of ozone, sampling a range of Jacobi angles. However, the interpretation of the polarization parameters for the slow fragments is made particularly difficult by the number of surfaces of different multiplicities that correlate with the triplet products.

C. Angular momentum orientation

The speed dependent values of γ'_1 recorded for $O(^3P_1)$ and $O(^3P_2)$ products are shown in Fig. 6. Interestingly, the high speed values of γ'_1 are the largest of the polarization parameters measured for the triplet channel. This large orientation moment is mirrored by a relatively large coherent alignment parameter γ_2 . Notice, however, that once transformed into the molecular frame, the orientation moments, given by $\text{Im}[\rho_{11}]$ in Figs. 9 and 10, are of similar magnitude to the corresponding alignment moments for the $J=1$ and 2 products. The speed dependence of the γ'_1 parameter is reminiscent of that measured by Lee *et al.* for the $O(^1D_2)$ fragments generated subsequent to dissociation of ozone in the Hartley band.⁵⁴ In both cases, the parameter is large and negative at high velocities and becomes smaller and eventually zero at low velocities. Lee *et al.* interpreted the large value of γ'_1 at high velocities in terms of static coherence,⁵⁴ while the zero value reported at low velocities was thought to be a result of adiabatic dissociation on the \tilde{A} state quenching the orbital orientation. It is possible that a similar effect is at play for the triplet channel, in accordance with the dissociation mechanisms proposed in Sec. IV A, and might also account in part for the rather small alignment parameters observed for the slow fragments. However, nonzero γ'_1 values may also be consistent with the predictions of the long-range interaction model for products emerging on either the \tilde{R} or the \tilde{X} surfaces at nonlinear configurations, and the correct interpretation of this parameter must await a more complete theoretical analysis. Such an analysis would almost certainly need to take into full account the coupling of the spin and orbital angular momenta in the exit channel. It should be noted that the simple adiabatic correlations discussed in Sec. IV A, on the other hand, only deal with incoherent terms of the angular momentum distribution and cannot, therefore, be used to rationalize the coherent orientation term discussed here.

V. CONCLUSIONS

Speed distributions, spatial anisotropy parameters, and atomic angular momentum polarization parameters have been measured for the $O(^3P_J)$ products subsequent to the dissociation of ozone at 248 and 226 nm. Building on previous interpretations, the data are shown to be consistent with two distinct dissociation mechanisms leading to fast and slow photofragments. In both cases, excitation is believed to occur to the \tilde{B} state. A major portion of the wavepacket then crosses to the \tilde{R} surface, generating fast fragments in a range of vibrational states, as supported by the quasiclassical trajectory calculations of Qu *et al.*²⁹ Furthermore, the data can be interpreted in terms of prompt recoil from a geometry close to that of the ground state at equilibrium. For the slow

fragments it is proposed that, following excitation to the \tilde{B} state, the system crosses onto the \tilde{A} state. The crossing seam is only accessible to parent molecules that are highly vibrationally excited and, therefore, possess modest speeds perpendicular to the surface crossing. Once on the \tilde{A} state, flux is drawn to the region around the D_{3h} well, where there is a nearby conical intersection with the ground electronic state. The wavepacket is thought to funnel through to the ground state, where it experiences a bond opening torque on its way to the ground state product asymptote. The velocity distributions, β parameters, and spin-orbit populations all appear consistent with this mechanism. The polarization of the angular momentum is thought also to be consistent with this picture, but its interpretation, particularly for the slow products, is made difficult by the numerous accessible potential energy surfaces in the long-range region.

ACKNOWLEDGMENTS

We gratefully acknowledge the EPSRC for research grants. We thank Professor G. Hancock and Dr G. A. D. Ritchie for supplying us with the ozone used in these experiments. It is also a pleasure to thank Professor Reinhard Schinke for valuable discussions.

- ¹C. E. Fairchild, E. J. Stone, and G. M. Lawrence, *J. Chem. Phys.* **69**, 3632 (1978).
- ²J. C. Brock and R. T. Watson, *Chem. Phys. Lett.* **71**, 371 (1980).
- ³R. K. Sparks, L. R. Carlson, K. Shobatake, M. L. Kowalczyk, and Y. T. Lee, *J. Chem. Phys.* **72**, 1401 (1980).
- ⁴S. T. Amimoto, A. P. Force, J. R. Wiesenfeld, and R. H. Young, *J. Chem. Phys.* **79**, 1244 (1980).
- ⁵A. A. Turnipseed, G. L. Vaghjani, T. Gierczak, J. E. Thompson, and A. R. Ravishankara, *J. Chem. Phys.* **95**, 3244 (1991).
- ⁶P. J. Hay, R. T. Pack, R. B. Walker, and E. J. Heller, *J. Phys. Chem.* **86**, 862 (1982).
- ⁷J. M. Price, J. A. Mack, C. A. Rogaski, and A. M. Wodtke, *Chem. Phys.* **175**, 83 (1993).
- ⁸C. A. Rogaski, J. M. Price, J. A. Mack, and A. M. Wodtke, *Geophys. Res. Lett.* **20**(24), 2885, 1993.
- ⁹R. Toumi, P. L. Houston, and A. M. Wodtke, *J. Chem. Phys.* **104**, 775 (1996).
- ¹⁰R. L. Miller, A. G. Suits, P. L. Houston, R. Toumi, J. A. Mack, and A. M. Wodtke, *Science* **265**, 1831 (1994).
- ¹¹J. A. Syage, *J. Phys. Chem.* **99**, 16530 (1995).
- ¹²J. A. Syage, *J. Phys. Chem.* **100**, 13885 (1996).
- ¹³J. A. Syage, *J. Chem. Phys.* **105**, 1007 (1996).
- ¹⁴R. J. Wilson, J. A. Mueller, and P. L. Houston, *J. Phys. Chem. A* **101**, 7593 (1997).
- ¹⁵K. Takahashi, N. Taniguchi, Y. Matsumi, and M. Kawasaki, *Chem. Phys.* **231**, 171 (1998).
- ¹⁶K. M. Hickson, P. Sharkey, I. W. M. Smith, A. C. Symonds, R. P. Tuckett, and G. N. Ward, *J. Chem. Soc., Faraday Trans.* **94**, 533 (1998).
- ¹⁷J. D. Geiser, S. M. Dylewski, J. A. Mueller, R. J. Wilson, R. Toumi, and P. L. Houston, *J. Chem. Phys.* **112**, 1279 (2000).
- ¹⁸P. L. Houston, B. R. Cosofret, A. Dixit, S. M. Dylewski, J. D. Geiser, J. A. Mueller, R. J. Wilson, P. J. Pisano, M. S. Westley, K. T. Lorenz, and D. W. Chandler, *J. Chin. Chem. Soc. (Taipei)* **48**, 309 (2001).
- ¹⁹P. J. Crutzen, J. U. Grob, C. Brühl, R. Müller, and J. M. Russell, *Science* **268**, 705 (1995).
- ²⁰J. U. Grob, R. Müller, G. Becker, D. S. McKenna, and F. J. Crutzen, *J. Atmos. Chem.* **34**, 171 (1999).
- ²¹M. Natarajan, E. E. Remsberg, and L. L. Gordley, *Geophys. Res. Lett.* **29**(7), 1152, 2002.
- ²²T. Canty, H. M. Pickett, R. J. Salawitch, K. W. Jucks, W. A. Traub, and J. W. Waters, *Geophys. Res. Lett.* **33**, L12802, 2006.
- ²³T. Kinugawa, T. Sato, T. Arikawa, Y. Matsumi, and M. Kawasaki, *J. Chem. Phys.* **93**, 3289 (1990).
- ²⁴H. Park and G. Slanger, *J. Chem. Phys.* **100**, 287 (1994).
- ²⁵M. J. Daniels and J. R. Wiesenfeld, *J. Chem. Phys.* **98**, 321 (1993).
- ²⁶S. M. Shamsuddin, Y. Inagaki, Y. Matsumi, and M. Kawasaki, *Can. J. Chem.* **72**, 637 (1994).
- ²⁷S. Y. Grebenshchikov, Z. W. Qu, H. Zhu, and R. Schinke, *Phys. Chem. Chem. Phys.* **9**, 2044 (2007).
- ²⁸M. Svanberg, J. B. C. Pettersson, and D. Murtagh, *J. Chem. Phys.* **102**, 8887 (1995).
- ²⁹Z.-W. Qu, H. Zhu, S. Y. Grebenshchikov, and R. Schinke, *J. Chem. Phys.* **122**, 191102 (2005).
- ³⁰C. Leforestier and F. LeQuéré, *J. Chem. Phys.* **101**, 3806 (1994).
- ³¹B. R. Johnson and J. L. Kinsey, *Phys. Rev. Lett.* **62**, 1607 (1989).
- ³²B. R. Johnson and J. L. Kinsey, *J. Chem. Phys.* **91**, 7638 (1989).
- ³³G. Parlant, *J. Chem. Phys.* **112**, 6956 (2000).
- ³⁴S. C. Farantos, *Chem. Phys.* **159**, 329 (1992).
- ³⁵Z. W. Qu, H. Zhu, and R. Schinke, *Chem. Phys. Lett.* **377**, 359 (2003).
- ³⁶P. Rosmus, P. Palmieri, and R. Schinke, *J. Chem. Phys.* **117**, 4871 (2002).
- ³⁷M. Tashiro and R. Schinke, *J. Chem. Phys.* **119**, 10186 (2003).
- ³⁸A. T. J. B. Eppink and D. H. Parker, *Rev. Sci. Instrum.* **68**, 3477 (1997).
- ³⁹D. W. Chandler and P. L. Houston, *J. Chem. Phys.* **87**, 1445 (1987).
- ⁴⁰M. Bass, M. Brouard, A. P. Clark, and C. Vallance, *J. Chem. Phys.* **117**, 8723 (2002).
- ⁴¹M. Brouard, A. P. Clark, C. Vallance, and O. S. Vasyutinskii, *J. Chem. Phys.* **119**, 771 (2003).
- ⁴²M. J. Bass, M. Brouard, A. P. Clark, B. Martínez-Haya, and C. Vallance, *Phys. Chem. Chem. Phys.* **5**, 856 (2003).
- ⁴³M. Brouard, R. Cireasa, A. P. Clark, T. J. Preston, C. Vallance, G. C. Groenenboom, and O. S. Vasyutinskii, *J. Phys. Chem. A* **108**, 7965 (2004).
- ⁴⁴M. Brouard, R. Cireasa, A. P. Clark, T. J. Preston, and C. Vallance, *J. Chem. Phys.* **124**, 064309 (2006).
- ⁴⁵M. Brouard, R. Cireasa, A. P. Clark, F. Quadrini, and C. Vallance, *Phys. Chem. Chem. Phys.* **8**, 5549 (2006).
- ⁴⁶M. Brouard, R. Cireasa, A. P. Clark, G. C. Groenenboom, G. Hancock, S. J. Horrocks, F. Quadrini, G. A. D. Ritchie, and C. Vallance, *J. Chem. Phys.* **125**, 133308 (2006).
- ⁴⁷B. Buijsse, A. T. J. B. Eppink, S. T. Gibson, B. R. Lewis, D. H. Parker, and W. J. van der Zande, *J. Chem. Phys.* **108**, 7229 (1998).
- ⁴⁸B. Y. Chang, R. C. Hoetzlein, J. A. Mueller, J. D. Geiser, and P. L. Houston, *Rev. Sci. Instrum.* **69**, 1665 (1998).
- ⁴⁹A. S. Bracker, E. R. Wouters, A. G. Suits, and O. S. Vasyutinskii, *J. Chem. Phys.* **110**, 6749 (1999).
- ⁵⁰L. D. A. Siebbeles, M. Glass-Maujean, O. S. Vasyutinskii, J. A. Beswick, and O. Roncero, *J. Chem. Phys.* **100**, 3610 (1994).
- ⁵¹T. P. Rakitzis and R. N. Zare, *J. Chem. Phys.* **110**, 3341 (1999).
- ⁵²B. V. Pichayev, A. G. Smolin, and O. S. Vasyutinskii, *J. Phys. Chem.* **101**, 7614 (1997).
- ⁵³A. G. Smolin, O. S. Vasyutinskii, E. R. Wouters, and A. G. Suits, *J. Chem. Phys.* **121**, 6759 (2004).
- ⁵⁴S. K. Lee, D. Townsend, O. S. Vasyutinskii, and A. G. Suits, *Phys. Chem. Chem. Phys.* **7**, 1650 (2005).
- ⁵⁵A. P. Clark, M. Brouard, F. Quadrini, and C. Vallance, *Phys. Chem. Chem. Phys.* **8**, 5591 (2006).
- ⁵⁶A. J. Alexander, *J. Chem. Phys.* **118**, 6234 (2003).
- ⁵⁷A. P. Clark, R. Cireasa, M. Brouard, F. Quadrini, and C. Vallance, in *Gas Phase Molecular Reaction and Photodissociation Dynamics*, edited by P. D. Kleiber and K. C. Lin (Transworld Research Network, Kerala), in press.
- ⁵⁸M. Brouard, A. V. Green, F. Quadrini, and C. Vallance, *J. Chem. Phys.* **127**, 084304 (2007).
- ⁵⁹M. Brouard, F. Quadrini, and C. Vallance, *J. Chem. Phys.* **127**, 084305 (2007).
- ⁶⁰M. C. G. N. van Vroonhoven and G. C. Groenenboom, *J. Chem. Phys.* **116**, 1965 (2002).
- ⁶¹NIST Atomic Spectra Database, version 3, 2005 (<http://physics.nist.gov/PhysRefData/ASD/index.html>).
- ⁶²H. S. W. Massey, *Rep. Prog. Phys.* **12**, 248 (1948).
- ⁶³R. Schinke, S. Y. Grebenshchikov, M. V. Ivanov, and P. Fleurat-Lessard, *Annu. Rev. Phys. Chem.* **57**, 625 (2006).
- ⁶⁴N. Sukumar and S. D. Peyerimhoff, *Mol. Phys.* **95**, 67 (1998).
- ⁶⁵R. Siebert, P. Fleurat-Lessard, R. Schinke, M. Bittererová, and S. C. Farantos, *J. Chem. Phys.* **116**, 9749 (2002).
- ⁶⁶G. J. Atchity and K. Ruedenberg, *Theor. Chem. Acc.* **96**, 176 (1997).

- ⁶⁷G. J. Atchity and K. Ruedenberg, *Theor. Chem. Acc.* **96**, 195 (1997).
- ⁶⁸Z.-W. Qu, H. Zhu, and R. Schinke, *J. Chem. Phys.* **123**, 204324 (2005).
- ⁶⁹E. Baloitcha and G. G. Balint-Kurti, *J. Chem. Phys.* **123**, 014306 (2005).
- ⁷⁰Z.-W. Qu, H. Zhu, S. Y. Grebenshchikov, and R. Schinke, *J. Chem. Phys.* **123**, 074305 (2005).
- ⁷¹B. R. Johnson, B.-Y. Chang, C.-W. Hsiao, L. Le, and J. L. Kinsey, *J. Chem. Phys.* **108**, 7670 (1998).
- ⁷²E. Baloitcha and G. G. Balint-Kurti, *Phys. Chem. Chem. Phys.* **7**, 3829 (2005).
- ⁷³M. H. Palmer and A. D. Nelson, *Mol. Phys.* **100**, 3601 (2002).
- ⁷⁴H. Zhu, Z.-W. Qu, M. Tashiro, and R. Schinke, *Chem. Phys. Lett.* **384**, 45 (2004).
- ⁷⁵J. M. Teule, G. C. Groenenboom, D. W. Neyer, D. W. Chandler, and M. H. M. Janssen, *Chem. Phys. Lett.* **320**, 177 (2000).
- ⁷⁶M. Ahmed, A. S. Bracker, D. S. Peterka, A. G. Suits, O. S. Vasyutinskii, and E. R. Wouters, in *Imaging in Chemical Dynamics*, ACS Symposium Series Vol. 770, edited by A. G. Suits and R. E. Continetti (American Chemical Society, Washington, DC, 2000).